Ultrahigh supercurrent density in a two-dimensional topological material

Qi Zhang,[1,*,†] Md. Shafayat Hossain ●,[1,*,‡] Brian Casas,[2] Wenkai Zheng,[2] Zi-Jia Cheng,[1] Zhuangchai Lai,[3,4] Yi-Hsin Tu,[5] Guoqing Chang,[6] Yao Yao,[3] Siyuan Li,[3] Yu-Xiao Jiang,[1] Sougata Mardanya,[5] Tay-Rong Chang,[5,7,8] Jing-Yang You,[9] Yuan-Ping Feng,[9,10] Guangming Cheng,[11] Jia-Xin Yin,[1] Nana Shumiya,[1] Tyler A. Cochran,[1] Xian P. Yang,[1] Maksim Litskevich,[1] Nan Yao,[11] Kenji Watanabe,[12] Takashi Taniguchi,[13] Hua Zhang,[3,14,15,§] Luis Balicas,[2] and M. Zahid Hasan[1,16,‖]

[1]*Laboratory for Topological Quantum Matter and Advanced Spectroscopy (B7), Department of Physics, Princeton University, Princeton, 08544 New Jersey, USA*
[2]*National High Magnetic Field Laboratory, Tallahassee, Florida 32310, USA*
[3]*Department of Chemistry, City University of Hong Kong, Hong Kong, China*
[4]*Department of Applied Physics, The Hong Kong Polytechnic University, Hong Kong, China*
[5]*Department of Physics, National Cheng Kung University, 701 Tainan, Taiwan*
[6]*Division of Physics and Applied Physics, School of Physical and Mathematical Sciences, Nanyang Technological University, Singapore 637371, Singapore*
[7]*Center for Quantum Frontiers of Research and Technology (QFort), 701 Tainan, Taiwan*
[8]*Physics Division National Center for Theoretical Sciences, 10617 Taipei, Taiwan*
[9]*Department of Physics, National University of Singapore, 2 Science Drive 3, Singapore 117551, Singapore*
[10]*Centre for Advanced 2D Materials, National University of Singapore, 6 Science Drive 2, Singapore 117546, Singapore*
[11]*Princeton Institute for Science and Technology of Materials, Princeton University, Princeton, 08544 New Jersey, USA*
[12]*Research Center for Functional Materials, National Institute for Materials Science, Tsukuba, Japan*
[13]*International Center for Materials Nanoarchitectonics, National Institute for Materials Science, Tsukuba, Japan*
[14]*Hong Kong Branch of National Precious Metals Material Engineering Research Center (NPMM), City University of Hong Kong, Hong Kong, China*
[15]*Shenzhen Research Institute, City University of Hong Kong, Shenzhen 518057, China*
[16]*Lawrence Berkeley National Laboratory, Berkeley, California 94720, USA*

Ongoing advances in superconductors continue to revolutionize technology thanks to the increasingly versatile and robust availability of lossless supercurrents. In particular, high supercurrent density can lead to more efficient and compact power transmission lines, high-field magnets, as well as high-performance nanoscale radiation detectors and superconducting spintronics. Here, we report the discovery of an unprecedentedly high superconducting critical current density ($17 \, \text{MA/cm}^2$ at 0 T and $7 \, \text{MA/cm}^2$ at 8 T) in $1\text{T}'\text{-WS}_2$, exceeding those of all reported two-dimensional superconductors to date. $1\text{T}'\text{-WS}_2$ features a strongly anisotropic (both in- and out-of-plane) superconducting state that violates the Pauli paramagnetic limit signaling the presence of unconventional superconductivity. Spectroscopic imaging of the vortices further substantiates the anisotropic nature of the superconducting state. More intriguingly, the normal state of $1\text{T}'\text{-WS}_2$ carries topological properties. The band structure obtained via angle-resolved photoemission spectroscopy and first-principles calculations points to a Z_2 topological invariant. The concomitance of topology and superconductivity in $1\text{T}'\text{-WS}_2$ establishes it as a topological superconductor candidate, which is promising for the development of quantum computing technology.

Since the discovery of superconductivity by Heike Kamerlingh Onnes [1] back in 1911, superconductors have revolutionized science and technology through numerous applications, ranging from superconducting qubits to high-field magnets [2–4]. High-field magnets fabricated from superconductors with high critical current density have enabled scientific discoveries across the physical, chemical, and biological sciences [5–7]. On the other hand, superconducting materials exhibiting topological properties offer possibilities beyond this classical application paradigm, opening a new frontier to implement fault-tolerant quantum information technologies. Recently, two-dimensional (2D) transition metal dichalcogenides (TMDCs) attracted considerable interests thanks to their abundant crystal structures and novel physical properties [8–11]. Specifically, hole-doped TMDCs have been considered as candidates for topological superconductivity based on momentum-space-split spinless fermions [8]. For example, the coexistence of superconductivity with a topologically nontrivial electronic state makes 2M-WS_2 a good candidate for topological superconductivity [12]. In this

————
*These authors contributed equally to this work.
†qz9@princeton.edu
‡mdsh@princeton.edu
§hua.zhang@cityu.edu.hk
‖mzhasan@princeton.edu

work, we utilized transport, spectroscopy, and microscopy techniques to showcase the unprecedentedly high superconducting critical current density and topological properties of the 2D superconductor 1T′-WS$_2$. Transport measurements reveal the twofold symmetry of the in-plane critical field, which is further confirmed by the anisotropic vortices imaged using scanning tunneling microscopy (STM). STM analysis helped identify the direction along which the vortices were most elongated, which correlates to the direction along which the upper critical magnetic field is expected to be small. This directional dependency is critical to leverage high critical current density at finite magnetic fields because the high critical current density can be maintained even at large magnetic fields as long as the field is applied along a specific crystallographic direction. Moreover, our theoretical calculations and angle-resolved photoemission spectroscopy (ARPES) data demonstrate that 1T′-WS$_2$ is a topological material, highlighting its potential as a promising candidate for next-generation quantum devices where a high supercurrent can be interfaced with topology, making the coexistence of both properties favorable for broader sets of applications.

1T′-WS$_2$ is composed of a distorted [WS$_6$] octahedral and crystallizes in a monoclinic layered structure [13], as shown in Fig. 1(a). High-purity 1T′-WS$_2$ crystals were synthesized via a previously reported method [13]. The single-phase nature can be observed in the cross-sectional scanning transmission electron microscope (STEM) image [Fig. 1(b)]. The STEM image unveils the atomic stacking pertaining to a monoclinic and distorted structure. This atomic-resolution characterization confirms the high crystallinity and phase purity of the as-synthesized 1T′-WS$_2$ crystals, consistent with the previous report [13]. After characterizing the bulk material, we fabricated devices based on few-layer 1T′-WS$_2$ for transport measurements. Thin flakes of 1T′-WS$_2$ obtained via mechanical exfoliation were transferred onto a SiO$_2$ (285-nm)/silicon substrate (Supplemental Material Fig. S1(a), inset [36]). The Raman spectrum of the as-prepared 1T′-WS$_2$ flake shows a series of peaks at ~112, ~178, ~270, ~316, and ~407 cm^{-1} (Supplemental Material Fig. S1(a) [36]), consistent with single-phase 1T′-WS$_2$ [13]. The thickness (d) of the flakes used in our measurements is ~6.1 nm as measured by the atomic force microscope (Supplemental Material Fig. S1(b) [36]). The device was fabricated following a Hall bar configuration and measured from T = 300 K to 2.0 K in a Physical Property Measurement System. Figure 1(c) depicts the four-probe resistance as a function of temperature and captures the electrical transport behavior of the sample. At high temperatures, it exhibits metallic behavior ($dR/dT > 0$), indicating phonon-scattering-dominated transport [14]. The superconducting transition occurs at 7.7 K, which is slightly lower than the bulk critical temperature (T_c) of 1T′-WS$_2$ (8.6 K) [13]. We also measured the Hall effect of 1T′-WS$_2$ above the critical temperature. Strikingly, the carrier concentration in 1T′-WS$_2$ approaches 10^{15} to 10^{16} cm^{-2} at T = 10 K (Supplemental Material Fig. S2(a) and (b) [36]). This value is much higher than the typical carrier concentration (~10^{14} cm^{-2}) of 2D superconductors with electrostatic gating [15].

To investigate the superconducting state of 1T′-WS$_2$, we performed magnetotransport measurements [Fig. 1(d)]. We start with the angular dependence of the upper critical

magnetic field (H_{c2}), defined as the magnetic field at which the resistance drops to 50% of its normal state value. The details of the angular dependent measurement are described in Supplemental Material Fig. S3 [36]. For a clear visualization, we normalized the resistance by R_n, i.e., the normal state resistance for all the samples. Figure 1(e) summarizes the magnetic field dependence of the resistance at different angles (θ) at T = 0.33 K, where θ is the angle between the z-axis and the magnetic field direction [Fig. 1(d)]. As the sample is rotated from the perpendicular ($\theta = 0°$) to a parallel ($\theta = 90°$) field configuration, the transition toward superconductivity progressively shifts to higher fields, manifesting a clear superconducting anisotropy [Fig. 1(e)]. In Fig. 1(f), we present a plot of H_{c2} as a function of θ, showing that the highest H_{c2} occurs when the magnetic field is applied parallel to the sample plane. To understand the anisotropic nature of H_{c2}, we fitted our data to the Tinkham formula, which describes the angular dependence of H_{c2} for a 2D superconductor [16]:

$$\left| \frac{H_{c2}(\theta) \cos\theta}{H_{c2,\perp}} \right| + \left(\frac{H_{c2}(\theta) \sin\theta}{H_{c2,//}} \right)^2 = 1, \tag{1}$$

where $H_{c2,\perp}$ and $H_{c2,//}$ are the upper critical field for fields perpendicular and parallel to the plane of the sample, respectively. As shown in Fig. 1(f), the blue fitting curve matches the data quite well and thus confirms the 2D nature of the superconductivity in 1T′-WS$_2$. The fitting of the angle-dependent critical field for smaller angular regimes to the 2D Tinkham formula is shown in Supplemental Material Fig. S4 [36].

After exploring the anisotropy of H_{c2} along the out-of-plane directions, we then examined how H_{c2} evolved along the in-plane directions. As the device is rotated from the x-axis [$\varphi = 0°$; φ is the angle between the magnetic field and the x-axis as shown in Fig. 1(d)] to the y-axis ($\varphi = 90°$), the superconducting transition progressively shifts from higher fields to lower fields [Fig. 1(g)]. Careful measurements were performed to rule out the possibility of an accidental out-of-plane component (Supplemental Material Fig. S5 [36]). Such a planar anisotropy is likely to result from the reduced crystal symmetry due to the distorted structure of 1T′-WS$_2$, as clearly seen in Fig. 1(a). Figure 1(h), which shows H_{c2} as a function of φ, reveals an emergent twofold symmetry. Furthermore, we observed that the largest value of the in-plane H_{c2} is 28 T. To obtain a quantitative understanding of such a large value, we compared it to the expected Pauli paramagnetic limiting field. In conventional superconductors, a sufficiently high external magnetic field can suppress superconductivity through the orbital [17] and spin Zeeman [18,19] effects. For a few-layer sample, the suppression from the orbital effect is nearly absent when the magnetic field is parallel to the sample plane. Consequently, the Zeeman effect imposes an upper bound on H_{c2}, known as the Pauli limit ($H_p = 1.84 \times T_c$ T/K) [20]. We find that the in-plane H_{c2} (28 T) in 1T′-WS$_2$ clearly violates the Pauli limit (14 T for T_c = 7.7 K). Such a violation combined with the emergence of twofold symmetry for the in-plane H_{c2} suggest unconventional superconductivity in 1T′-WS$_2$.

We further explored the superconducting transition via systematic temperature-dependent measurements. Figure 1(i) and 1(j) shows such data taken when the magnetic field was perpendicular and parallel to the sample plane, respectively.
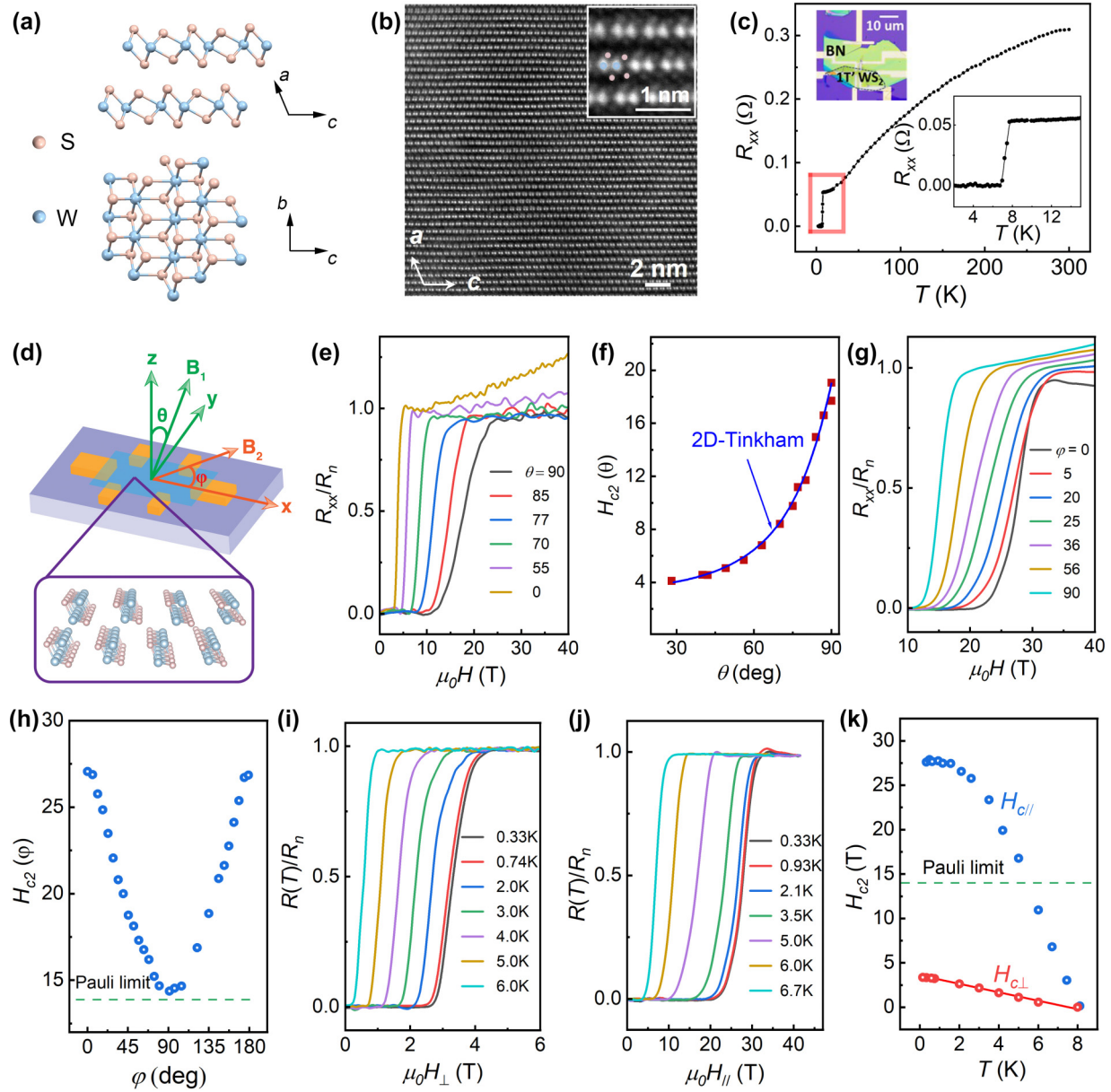
FIG. 1. Crystal structure and superconductivity of 1T′-WS₂. (a) Schematic illustration of the structure of 1T′-WS₂. Top panel: side view of the crystallographic structure; bottom panel: top view of a typical monolayer. (b) Cross-sectional STEM image of 1T′-WS₂. Inset: high-magnification STEM image of layered structure with atomic resolution. (c) Temperature-dependent electrical resistance of the mechanically exfoliated 1T′-WS₂ without magnetic field. Insets: optical image of the 1T′-WS₂ device covered by h-BN with a Hall bar configuration (top) and a small-range $R_{xx} - T$ plot of 1T′-WS₂ around T_c shown in the area within the red rectangle (bottom). (d) Schematic illustration of a 1T′-WS₂ device and the rotation experiment setup, where the x-axis is parallel to the c-axis of the crystal and the z-axis is perpendicular to the crystalline plane. θ is the angle between the out-of-plane magnetic field and the z-axis; φ is the angle between the in-plane magnetic field and the axis with largest in-plane critical field. (e) Magnetic field dependence of the normalized resistance of the 1T′-WS₂ device at $T = 0.33$ K with different out-of-plane rotation angles θ. (f) The θ dependence of the upper critical field. The blue curve denotes a fit to the data following the Tinkham formula for a 2D superconductor. (g) Magnetic field dependence of the normalized resistance of the 1T′-WS₂ device at $T = 0.33$ K with different in-plane rotation angles φ. (h) The φ dependence of the upper critical field. The green dashed line indicates the Pauli limit. (i) and (j) Superconducting transition of the 1T′-WS₂ device under a perpendicular magnetic field (i) and under a parallel magnetic field (j) at different temperature. (k) Temperature dependence of the upper critical field with magnetic field directions parallel and perpendicular to the crystal plane. The red line represents the linear relationship between $H_{c2,\perp}$ and T according to the 2D GL theory.

In both cases, the superconducting transition shifts gradually to lower magnetic fields as the temperature increases. The temperature dependence of the out-of-plane upper critical field ($H_{c2,\perp}$) and the in-plane upper critical field ($H_{c2,//}$) are summarized in Fig. 1(k). $H_{c2,\perp}$ displays a linear dependence

on temperature that is well fitted by the standard Ginzburg-Landau (GL) theory for 2D superconductors [16]:

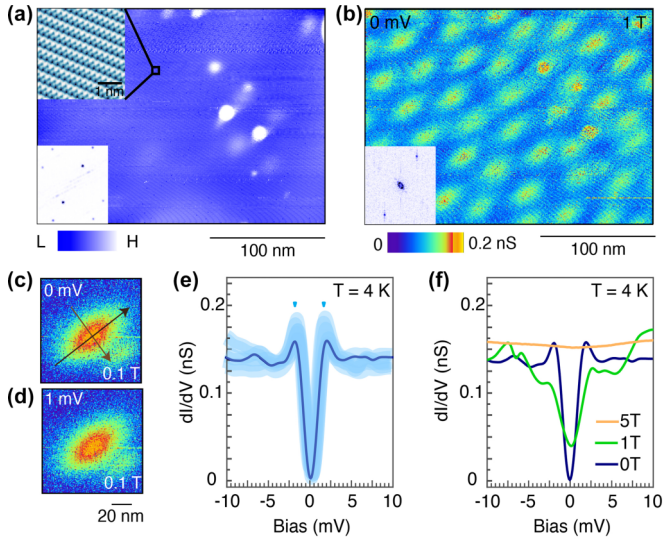$$H_{c2,\perp}(T) = \frac{\Phi_0}{2\pi \xi_{GL}(0)^2}\left(1 - \frac{T}{T_c}\right), \qquad (2)$$

FIG. 2. Scanning tunneling microscopy measurements on 1T′-WS₂. (a) Topographic image of the *bc* plane of 1T′-WS₂. Top inset: a zoom-in view of the topographic image showing the atomic arrangements. Bottom inset: fast Fourier transform of the topographic image. (b) A zero-bias conductance map of vortices at 1 T. Inset: Fourier transform of the *dI/dV* map. (c) and (d) The conductance map of a single vortex at 1 T with zero bias (c) and 1-mV bias (d). (e) Tunneling spectroscopy spectrum taken at 4.2 K, revealing a superconducting gap. Light blue curves are the differential spectra taken at different positions on the surface; the dark blue curve denotes the average spectra. (f) Field dependence of tunneling spectroscopy taken at 0 T, 1 T, and 5 T.

where $\xi_{GL}(0)$ is the zero-temperature GL in-plane coherence length, Φ_0 is the magnetic flux quantum, and T_c is the critical temperature at which the resistance drops to 50% of its value in the normal state. From the fit, we can estimate the coherence length $\xi_{GL}(0) \approx 9.6$ nm. The temperature dependence of $H_{c2,//}$, on the other hand, follows the GL formula expected for 2D superconductors [16]:

$$H_{c2,//}(T) = \frac{\Phi_0\sqrt{3}}{\pi\xi_{GL}(0)d_{SC}}\left(1 - \frac{T}{T_c}\right)^{1/2}, \qquad (3)$$

where d_{SC} is the superconducting thickness. From the fitting of $H_{c2,//}$, the superconducting thickness is around 3.2 nm, which is smaller than $\xi_{GL}(0)$ and consistent with 2D superconductivity.

To investigate comprehensively the superconductivity properties in 1T′-WS₂ with microscopic and spectroscopic techniques, we performed STM measurements and directly imaged the vortices under magnetic field. A single crystal was cleaved *in situ* at $T = 77$ K and measured at $T = 4.2$ K. Figure 2(a) shows the topography of 1T′-WS₂ over a large area. The atomically resolved STM topographic image reveals a clean surface featuring zigzag chains along the *b*-axis of the crystal [Fig. 2(a), top inset]. In addition, the corresponding fast Fourier transform pattern also exhibits the distorted octahedral coordination feature [Fig. 2(a), bottom inset]. A zero-energy conductance map under 1 T applied perpendicularly to the *bc* plane is shown in Fig. 2(b). The Fourier transform of the *dI/dV* map is twofold symmetric [Fig. 2(b),

inset]. The conductance maps of a single vortex at 0.1 T taken at $V = 0$ mV [Fig. 2(c)] and 1 mV [Fig. 2(d)] further highlight the anisotropic nature of superconductivity. Consistent with the anisotropy observed in our transport data, the vortices are anisotropic and elongated along the specific direction, reflecting the anisotropy of the Ginzburg-Landau coherence length between both directions. By fitting the spatially resolved zero-bias conductance to $\Delta (r) = \Delta_0 \tanh(r/\xi)$ [21], where Δ_0 is the bulk energy gap, r is the radius from the vortex, and ξ is the coherence length, we obtain a range of coherence lengths from 7.583 nm to 37.3 nm. The polar diagram of in-plane coherence lengths is shown in Supplemental Material Fig. S6 [36]. Tunneling differential conductance collected from an atomically resolved lattice illustrates a superconducting gap with sharp coherence peaks [Fig. 2(e)]. This superconducting gap disappears gradually as the magnetic field is increased [Fig. 2(f)].

Subsequently, we performed critical current density (J_c) measurements. As alluded in the introduction, an important aspect of a superconductor is its J_c, which dictates several practical applications. The higher the J_c of a superconductor, the smaller and more efficient the superconducting devices that can be fabricated from it or the larger the magnetic fields that can be generated. We measured the differential resistance of the 1T′-WS₂ device with a thickness of 6 nm as a function of dc bias current at different temperatures [Fig. 3(a)]. Note that, I_c is defined as the current at which the differential resistance (dV/dI) reaches its maximum, as reported in previous works [22,23]. All of the critical current densities are calculated using the same definition (Supplemental Material Fig. S7 [36]), that is, $J_c = I_c/(W \times d)$. Remarkably, as seen in Fig. 3(b), T′-WS₂ exhibits ultrahigh critical current densities reaching $17\,\text{MA/cm}^2$ at $T = 0.33$ K. Figure 3(b) highlights the temperature dependence of the critical current density, featuring an enormous $J_c = 13\,\text{MA/cm}^2$ at liquid helium temperature (4.2 K). In addition, we systematically measured the critical currents of samples with different layer thicknesses, as shown in Supplemental Material Figs. S8 and S9 [36]. The thickness dependence of the critical current density is summarized in Fig. 3(c). There is no obvious difference among the samples with thicknesses exceeding 20 nm. The critical current densities increase as the devices become thinner, which is also observed in atomically thin TaS₂ [24]. Furthermore, we evaluated the field dependence of J_c (Supplemental Material Fig. S10 [36]). The critical current density falls rapidly as the perpendicular magnetic field increases [Fig. 3(d)]. In contrast, the critical current density is rarely influenced by a parallel magnetic field, since 1T′-WS₂ shows extremely high in-plane upper critical fields.

Experimentally, numerous 2D superconducting transition metal dichalcogenides have been studied [22–33]. In-plane anisotropic upper critical fields were observed in 2H-NbSe₂ [25] and T$_d$-MoTe₂ [26]. 2H-NbSe₂ [20] and ionic-gated 2H-MoS₂ [27] also exhibited high in-plane upper critical fields. However, we emphasize that 1T′-WS₂ is the only 2D material to our knowledge that shows the suitable critical temperature and high critical current under a high in-plane magnetic field, which are crucial for building high-field magnets. Even for a thick sample, the in-plane critical field surpasses 8 T at 4 K (Supplemental Material Fig. S11 [36]).
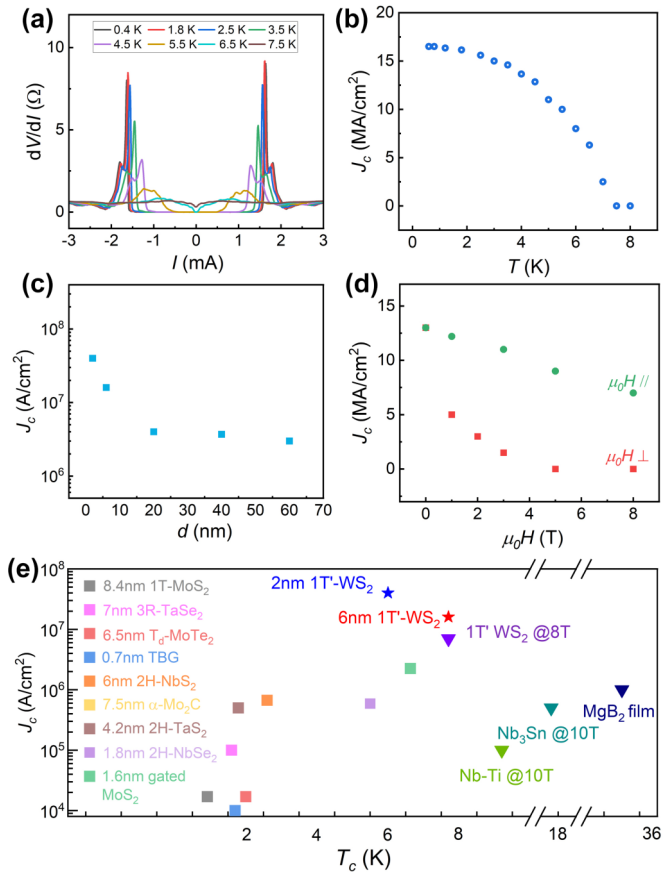
FIG. 3. Ultrahigh critical current density of $1T'$-WS_2. (a) Differential resistance of a 6-nm-thick $1T'$-WS_2 sample as a function of the dc bias at different temperatures. (b) Critical current density for a $1T'$-WS_2 device as a function of the temperature. (c) Critical current density of the $1T'$-WS_2 device plotted as a function of sample thickness. (d) Critical current densities of the $1T'$-WS_2 device plotted as a function of perpendicular and parallel magnetic fields. (e) Comparison of critical current densities among $1T'$-WS_2 and other representative 2D superconductors, such as twisted bilayer graphene (TBG) and transition metal dichalcogenides. Commercial magnet building materials are also included for reference. Here, the superconducting critical temperatures T_c of the different materials were determined under zero magnetic field.

We summarize the parameters of 2D superconductors in Fig. 3(e) and Supplemental Material Table SI [36]. As for $1T$-MoS_2 [28], $2H$-TaS_2 [24], $3R$-$TaSe_2$ [29], T_d-$MoTe_2$ [26], and $2H$-NbS_2 [23], their critical temperatures are below the temperature of liquid helium (4.2 K), rendering the construction of high-field magnets impractical. Gated MoS_2 displays a relatively high critical temperature and also very high critical fields, but superconductors under ionic gating are not suitable for applications [30]. Lastly, $2H$-$NbSe_2$ is comparable to $1T'$-WS_2 in critical fields and critical temperatures. However, its critical current density is two orders of magnitude lower than that of $1T'$-WS_2 [31]. The significance of our work is that we report an unprecedentedly high superconducting critical current density (17 MA/cm^2 at 0 T) in $1T'$-WS_2, which exceeds those of all the known 2D superconductors to date [21–33]. Notably, it even exceeds

the J_c of MgB_2 films [34], a well-known superconductor for high-critical-current applications [Fig. 3(e)]. Even under an 8 T in-plane magnetic field, the J_c of $1T'$-WS_2 is substantially large (7 MA/cm^2). As a reference, the critical currents of commercial magnet building materials are listed here, such as Nb-Ti alloy (0.1 MA/cm^2 at 10 T) and Nb_3Sn (0.5 MA/cm^2 at 10 T) [35]. The large J_c at zero and finite magnetic fields makes $1T'$-WS_2 a potential candidate for future study on building next-generation superconducting magnets.

Having explored the superconductivity of $1T'$-WS_2, we turn to the topological features pertinent to its electronic band structure using a series of theoretical calculations and ARPES experiments. The calculated bulk band structure is shown in Fig. 4(a). Besides the continuous energy gap between conduction band and valence band around the Fermi level, we observe a band inversion at the Γ-point between tungsten d and sulfur p orbitals, which leads to a strong topological insulating phase. Furthermore, the surface-projected calculation shows the topological Dirac surface state emerging from the valence band and merging into conduction bands [Fig. 4(b)]. The corresponding ARPES data [Fig. 4(c)], taken at $T = 10$ K (above T_c) matches the first-principles calculations below E_F. In particular, we identify the linear-dispersed hole pocket at Γ to be the lower cone of the topological surface state, as it shows no photon energy dependence and agrees well with the calculated dispersion of the Dirac state. (More details of ARPES data analysis are shown in Supplemental Material Figs. S12–S14 [36].) The ARPES Fermi surface map also visualizes the highly anisotropic Fermi surface [Fig. 4(d) and (e)], which possibly contributes to the extremely anisotropic H_{c2} in $1T'$-WS_2. The calculated superconducting gap of $1T'$-WS_2 on the Fermi surface is presented in Fig. 4(f) and Supplemental Material Fig. S15 [36]. These results lend crucial credence to the in-plane anisotropy of superconductivity. It is noted that high supercurrent may not be due to topology, but their simultaneous existence is favorable for broader sets of applications.

In summary, combining a series of experimental and numerical techniques, we comprehensively studied $1T'$-WS_2 and found a unique blend of ultrahigh critical supercurrent density, large superconducting anisotropy (in-plane versus out-of-plane), along with topological features. Our findings not only provide a promising material platform for high magnetic field technologies, but also unveil a promising platform for future exploration of topological superconductivity, which may be used to fabricate topologically protected qubits for future quantum computing schemes.
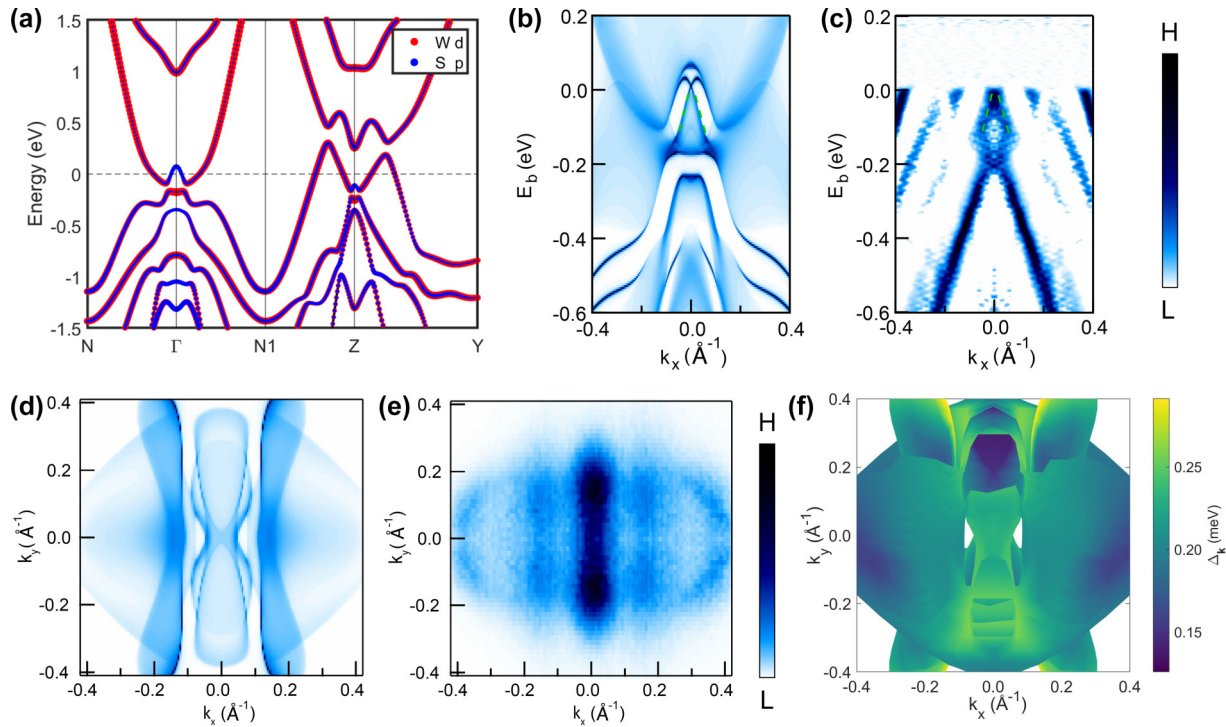
FIG. 4. Topological features of 1T′-WS$_2$. (a) Bulk band structure with spin-orbital coupling. The red and blue dots indicate tungsten d orbitals and sulfur p orbitals, respectively. (b) Calculated surface band structure of 1T′-WS$_2$ at $k_y = 0$, featuring a topological Dirac surface state near the Fermi level. (c) The second-derivative plot of the energy momentum cut at $k_y = 0$ acquired through ARPES. (d) Calculated Fermi surface. (e) Fermi surface of 1T′-WS$_2$ acquired through ARPES. (f) Top view of calculated superconducting gap in the surface Brillouin zone at 2.5 K on the Fermi surface.

[1] H. K. Onnes, The superconductivity of mercury, Commun. Phys. Lab 122 (1911).

[2] J. Bardeen, L. N. Cooper, and J. R. Schrieffer, Microscopic theory of superconductivity, Phys. Rev. **106**, 162 (1957).

[3] T. G. Berlincourt, Emergence of Nb-Ti as supermagnet material, Cryogenics **27**, 283 (1987).

[4] I. Siddiqi, Engineering high-coherence superconducting qubits, Nat. Rev. Mater. **6**, 875 (2021).

[5] Y. Zhang, Y. Tan, H. L. Stormer, and P. Kim, Experimental observation of the quantum Hall effect and Berry's phase in graphene, Nature (London) **438**, 201 (2005).

[6] M. A. Shampo, R. A. Kyle, and D. P. Steensma, Nobel Prize for nuclear magnetic resonance spectroscopy, Mayo Clin. Proc. **87**, e109 (2012).

[7] P. C. Lauterbur and P. Mansfield, Paul Lauterbur and Sir Peter Mansfield for MRI, Euro. Heart J. **40**, 1898 (2019).

[8] Y. Hsu, A. Vaezi, M. H. Fischer, and E. Kim, Topological superconductivity in monolayer transition metal dichalcogenides, Nat. Commun. **8**, 14985 (2017).

[9] S. Tang *et al.*, Quantum spin Hall state in monolayer 1T′-WTe$_2$, Nat. Phys. **13**, 683 (2017).

[10] P. Chen, W. Pai, Y.- H. Chan, W. L. Sun, C. Z. Xu, D. S. Lin, M. Y. Chou, A. V. Fedorov, and T. C. Chiang, Large quantum-

spin-Hall gap in single-layer 1T′ WSe$_2$, Nat. Commun. **9**, 2003 (2018).

[11] P. Li, Y. Wen, X. He, Q. Zhang, C. Xia, Z. Yu, S. A. Yang, Z. Zhu, H. N. Alshareef, and X. Zhang, Evidence for topological type-II Weyl semimetal WTe$_2$, Nat. Commun. **8**, 2150 (2017).

[12] Y. Fang, J. Pan, D. Zhang, D. Wang, H. T. Hirose, T. Terashima, S. Uji, Y. Yuan, W. Li, Z. Tian, J. Xue, Y. Ma, W. Zhao, Q. Xue, G. Mu, J. Zhang, and F. Huang, Discovery of superconductivity in 2M WS$_2$ with possible topological surface states, Adv. Mater. **31**, 1901942 (2019).

[13] Z. Lai *et al.*, Metastable 1T′-phase group VIB transition metal dichalcogenide crystals, Nat. Mater. **20**, 1113 (2021).

[14] T. Kawamura and S. D. Sarma, Phonon-scattering-limited electron mobilities in Al$_x$Ga$_{1-x}$As/GaAs heterojunctions, Phys. Rev. B **45**, 3612 (1992).

[15] J. T. Ye, Y. J. Zhang, R. Akashi, M. S. Bahramy, R. Arita, and Y. Iwasa, Superconducting dome in a gate-tuned band insulator, Science **338**, 1193 (2012).

[16] M. Tinkham, *Introduction to Superconductivity*, 3rd ed. (McGraw-Hill, New York, 1996).

[17] H. F. Hess, R. B. Robinson, R. C. Dynes, J. M. Valles Jr., and J. V. Waszczak, Scanning-Tunneling-Microscope Observation of the Abrikosov Flux Lattice and the Density of States Near and Inside a Fluxoid, Phys. Rev. Lett. **62**, 214 (1989).

[18] B. S. Chandrasekhar, A note on the maximum critical field of high-field superconductors, Appl. Phys. Lett. **1**, 7 (1962).

[19] A. M. Clogston, Upper Limit for Critical Field in Hard Superconductors, Phys. Rev. Lett. **9**, 266 (1962).

[20] X. Xi, Z. Wang, W. Zhao, J. Park, K. Law, H. Berger, L. Forró, J. Shan, and K. F. Mak, Ising pairing in superconducting NbSe$_2$ atomic layers, Nat. Phys. **12**, 139 (2016).

[21] J. E. Sonier, Investigations of the core structure of magnetic vortices in type-II superconductors using muon spin rotation, J. Phys. Condens. Matter **16**, S4499 (2004).

[22] C. Xu, L. Wang, Z. Liu, L. Chen, J. Guo, N. Kang, X. Ma, H. Cheng, and W. Ren, Large-area high-quality 2D ultrathin Mo$_2$C superconducting crystals, Nat. Mater. **14**, 1135 (2015).

[23] Z. Wang, C. Cheon, M. Tripathi, G. M. Marega, Y. Zhao, H. Ji, M. Macha, A. Radenovic, and A. Kis, Superconducting 2D NbS$_2$ grown epitaxially by chemical vapor deposition, ACS Nano **15**, 18403 (2021).

[24] E. Navarro-Moratalla, J. O. Island, S. Mañas-Valero, E. Pinilla-Cienfuegos, A. Castellanos-Gomez, J. Quereda, G. Rubio-Bollinger, L. Chirolli, J. Silva-Guillén, N. Agraït, G. A. Steele, F. Guinea, H. S. J. van der Zant, and E. Coronado, Enhanced superconductivity in atomically thin TaS$_2$, Nat. Commun. **7**, 11043 (2016).

[25] A. Hamill, B. Heischmidt, E. Sohn, D. Shaffer, K. Tsai, X. Zhang, X. Xi, A. Suslov, H. Berger, L. Forró, F. J. Burnell, J. Shan, K. F. Mak, R. M. Fernandes, K. Wang, and V. S. Pribiag, Two-fold symmetric superconductivity in few-layer NbSe$_2$, Nat. Phys. **17**, 949 (2021).

[26] J. Cui, P. Li, J. Zhou, W. He, X. Huang, J. Yi, J. Fan, Z. Ji, X. Jing, F. Qu, Z. G. Cheng, C. Yang, L. Lu, K. Suenaga, J. Liu, K. T. Law, J. Lin, Z. Liu, and G. Liu, Transport evidence of asymmetric spin-orbit coupling in few-layer superconducting 1T$_d$-MoTe$_2$, Nat. Commun. **10**, 2044 (2019).

[27] J. M. Lu, O. Zheliuk, I. Leermakers, N. F. Yuan, U. Zeitler, K. T. Law, and J. T. Ye, Evidence for two-dimensional Ising superconductivity in gated MoS$_2$, Science **350**, 1353 (2015).

[28] C. H. Sharma, A. P. Surendran, S. S. Varma, and M. Thalakulam, 2D superconductivity and vortex dynamics in 1T-MoS$_2$, Commun. Phys. **1**, 90 (2018).

[29] Y. Deng, Y. Lai, X. Zhao, X. Wang, C. Zhu, K. Huang, C. Zhu, J. Zhou, Q. Zeng, R. Duan, Q. Fu, L. Kang, Y. Liu, S. J. Pennycook, X. Renshaw Wang, and Z. Liu, Controlled growth of 3R phase tantalum diselenide and its enhanced superconductivity, J. Am. Chem. Soc. **142**, 2948 (2020).

[30] O. Zheliuk, J. M. Lu, Q. H. Chen, A. A. El Yumin, S. Golightly, and J. T. Ye, Josephson coupled Ising pairing induced in suspended MoS$_2$ bilayers by double-side ionic gating, Nat. Nanotechnol. **14**, 1123 (2019).

[31] N. Paradiso, A. T. Nguyen, K. E. Kloss, and C. Strunk, Phase slip lines in superconducting few-layer NbSe$_2$ crystals, 2D Mater. **6**, 025039 (2019).

[32] Y. Saito, J. Ge, K. Watanabe, T. Taniguchi, and A. F. Young, Independent superconductors and correlated insulators in twisted bilayer graphene, Nat. Phys. **16**, 926 (2020).

[33] Y. Ji, Y. Chu, A. Zhi, J. Tian, J. Tang, L. Liu, F. Wu, Y. Yuan, R. Yang, X. Tian, D. Shi, X. Bai, W. Yang, and G. Zhang, Enhanced critical field and anomalous metallic state in two-dimensional centrosymmetric 1T′-WS$_2$, Phys. Rev. B **105**, L161402 (2022).

[34] C. Eom *et al.*, High critical current density and enhanced irreversibility field in superconducting MgB$_2$ thin films, Nature (London) **411**, 558 (2001).

[35] P. J. Lee and D. C. Larbalestier, Microstructural factors important for the development of high critical current density Nb$_3$Sn strand, Cryogenics **48**, 283 (2008).

[36] See Supplemental Material at http://link.aps.org/supplemental/10.1103/PhysRevMaterials.7.L071801 for methods, more transport and ARPES data, and the details of calculations. References [37–51] are included therein.

[37] P. E. Blöchl, Projector augmented-wave method, Phys. Rev. B **50**, 17953 (1994).

[38] G. Kresse and D. Joubert, From ultrasoft pseudopotentials to the projector augmented-wave method, Phys. Rev. B **59**, 1758 (1999).

[39] G. Kresse and J. Furthmüller, Efficiency of ab-initio total energy calculations for metals and semiconductors using a plane-wave basis set, Comput. Mater. Sci. **6**, 15 (1996).

[40] J. P. Perdew, K. Burke, and M. Ernzerhof, Generalized Gradient Approximation Made Simple, Phys. Rev. Lett. **77**, 3865 (1996).

[41] A. A. Mostofi, J. R. Yates, Y. Lee, I. Souza, D. Vanderbilt, and N. Marzari, Wannier90: A tool for obtaining maximally-localised Wannier functions, Comput. Phys. Commun. **178**, 685 (2008).

[42] N. Marzari and D. Vanderbilt, Maximally localized generalized Wannier functions for composite energy bands, Phys. Rev. B **56**, 12847 (1997).

[43] P. Giannozzi, S. Baroni, N. Bonini, M. Calandra, R. Car, C. Cavazzoni, D. Ceresoli, G. L. Chiarotti, M. Cococcioni, and I. Dabo, QUANTUM ESPRESSO: A modular and open-source software project for quantum simulations of materials, J. Phys. Condens. Matter **21**, 395502 (2009).

[44] J. P. Perdew and A. Zunger, Self-interaction correction to density-functional approximations for many-electron systems, Phys. Rev. B **23**, 5048 (1981).

[45] A. Dal Corso, Pseudopotentials periodic table: From H to Pu, Comput. Mater. Sci. **95**, 337 (2014).

[46] M. Methfessel and A. T. Paxton, High-precision sampling for Brillouin-zone integration in metals, Phys. Rev. B **40**, 3616 (1989).

[47] S. Baroni, S. de Gironcoli, A. Dal Corso, and P. Giannozzi, Phonons and related crystal properties from density-functional perturbation theory, Rev. Mod. Phys. **73**, 515 (2001).

[48] F. Giustino, M. L. Cohen, and S. G. Louie, Electron-phonon interaction using Wannier functions, Phys. Rev. B **76**, 165108 (2007).

[49] S. Poncé, E. R. Margine, C. Verdi, and F. Giustino, EPW: Electron–phonon coupling, transport and superconducting properties using maximally localized Wannier functions, Comput. Phys. Commun. **209**, 116 (2016).

[50] E. R. Margine and F. Giustino, Anisotropic Migdal-Eliashberg theory using Wannier functions, Phys. Rev. B **87**, 024505 (2013).

[51] G. Pizzi *et al.*, Wannier90 as a community code: New features and applications, J. Phys. Condens. Matter **32**, 165902 (2020).